Turbulent Mixing in Shallow Trade Wind Cumuli: Dependence on Cloud Life Cycle

T. Schmeissner,* R. A. Shaw,[+] J. Ditas,[#] F. Stratmann,* M. Wendisch,[@] and H. Siebert*

*Leibniz Institute for Tropospheric Research (TROPOS), Leipzig, Germany
[+] Department of Physics, Michigan Technological University, Houghton, Michigan
[#] Multiphase Chemistry Department, Max Planck Institute for Chemistry, Mainz, Germany
[@] Leipzig Institute for Meteorology, Leipzig, Germany

ABSTRACT

Helicopter-borne observations of the impact of turbulent mixing and cloud microphysical properties in shallow trade wind cumuli are presented. The measurements were collected during the Cloud, Aerosol, Radiation and Turbulence in the Trade Wind Regime over Barbados (CARRIBA) project. Basic meteorological parameters (3D wind vector, air temperature, and relative humidity), cloud condensation nuclei concentrations, and cloud microphysical parameters (droplet number, size distribution, and liquid water content) are measured by the Airborne Cloud Turbulence Observation System (ACTOS), which is fixed by a 160-m-long rope underneath a helicopter flying with a true airspeed of approximately $20\,\mathrm{m\,s}^{-1}$. Clouds at different evolutionary stages were sampled. A total of 300 clouds are classified into actively growing, decelerated, and dissolving clouds. The mixing process of these cloud categories is investigated by correlating the cloud droplet number concentration and cubed droplet mean volume diameter. A significant tendency to more inhomogeneous mixing with increasing cloud lifetime is observed. Furthermore, the mixing process and its effects on droplet number concentration, droplet size, and cloud liquid water content are statistically evaluated. It is found that, in dissolving clouds, liquid water content and droplet number concentration are decreased by about 50% compared to actively growing clouds. Conversely, the droplet size remains almost constant, which can be attributed to the existence of a humid shell around the cloud that prevents cloud droplets from rapid evaporation after entrainment of premoistened air. Moreover, signs of secondary activation are found, which results in a more difficult interpretation of observed mixing diagrams.

1. Introduction

Shallow cumuli are the prevailing cloud type of the maritime trade wind region. Despite having diameters of less than 1 km, these small clouds play a major role in the maintenance of the tropical circulation, as they cover a large amount of the oceans (Riehl et al. 1951; Stevens 2005). They are important for the transport of heat, moisture, and momentum from the ocean surface to the free troposphere (e.g., Tiedtke 1989). At the same time, they influence boundary layer height and the vertical profiles of temperature, relative humidity, and wind (Bretherton et al. 2004).

Shallow trade wind cumuli have been studied for more than half a century (e.g., Stommel 1947; Malkus 1949; Warner 1955; Squires 1958). However, there are still numerous open questions with regard to their evolution and properties. One of them concerns the process of entraining subsaturated environmental air into the cloud and subsequent mixing with the cloudy air, which was first studied by Stommel (1947) and Squires and Warner (1957). The mixing process is described by the Damköhler number $\mathrm{Da} = \tau_t/\tau_p$, with τ_t being the turbulent mixing time scale and τ_p being the phase relaxation time describing the time required to achieve equilibrium vapor saturation because of the evaporation (or growth) of the entire droplet population (Baker and Latham 1979; Baker et al. 1980, 1984; Jensen and Baker 1989; Lehmann et al. 2009; Kumar et al. 2013). For $\mathrm{Da} \ll 1$ the turbulent mixing is fast, and the entire droplet population experiences nearly the same thermodynamic conditions. Therefore, this mixing type is called homogeneous. If τ_p is small compared to τ_t ($\mathrm{Da} \gg 1$) only

cloud droplets close to the mixing interface will be affected. This mixing type is called inhomogeneous, and in the literature it is sometimes also referred to as extremely inhomogeneous (e.g., Jensen and Baker 1989). The two mixing types generate a new thermodynamic environment, which influences droplet size D and droplet number concentration N in a variety of ways (Cooper 1989; Burnet and Brenguier 2007). Homogeneous mixing decreases D as well as N, whereas inhomogeneous mixing decreases only N, while D remains nearly constant. Therefore, the mixing process can be investigated by analyzing the Damköhler number or the resulting cloud droplet population (D, N), which is the method applied here.

The mixing type is crucial for the evolution of cloud microphysical properties, dynamics, lifetime, and optical properties (Brenguier et al. 2000; Grabowski 2006) and is of importance for the first indirect aerosol effect (e.g., Pawlowska et al. 2000).

Numerous observational and numerical studies have been performed to investigate the mixing process of shallow convective clouds. Up to now, there is no consensus about the prevailing mixing type in shallow cumuli. Some observations suggest that homogeneous mixing is dominant (e.g., Jensen et al. 1985; Jensen and Baker 1989). Others indicate the inhomogeneous mixing scenario as the prevailing process (e.g., Gerber 2006; Pawlowska et al. 2000). Some studies do not clearly differentiate between the mixing processes (e.g., Gerber et al. 2008). Small et al. (2013), Burnet and Brenguier (2007), and Lehmann et al. (2009) found both homogeneous and inhomogeneous mixing in shallow cumuli depending on the cloud location. Small et al. (2013) observed that the mixing tends toward the homogeneous scenario for upper parts of the clouds and is rather inhomogeneous in the lower cloud parts. Similar results were found in the modeling studies of Jarecka et al. (2013). Burnet and Brenguier (2007) and Lehmann et al. (2009) found some indication that the mixing process was connected to the dilution and, therefore, to the evolutionary stage of the clouds.

These findings motivated the current detailed study of the mixing process in shallow trade wind cumuli as a function of the cloud evolutionary stage. Observations of Katzwinkel et al. (2014) suggest three stages in shallow cumulus evolution: "actively growing," "decelerated," and "dissolving." This classification is based on updraft velocity and buoyancy in the cloud interior. Moreover, Fig. 8 of Katzwinkel et al. (2014) conceptually identifies large-scale dynamics of clouds, which are highly relevant for the microphysical response considered in this manuscript.

Data obtained during the Clouds, Aerosol, Radiation and Turbulence in the Trade Wind Regime over Barbados (CARRIBA) campaign (Siebert et al. 2013) are analyzed in this paper. CARRIBA is based on observations obtained by the helicopter-borne measurement payload Airborne Cloud Turbulence Observation System (ACTOS; Siebert et al. 2006a), plus a radiation measurements system (Werner et al. 2013, 2014). ACTOS yields high-resolution data of turbulence, thermodynamics, and cloud microphysical parameters. These high-resolution data were used to study the mixing process in shallow cumuli during different stages of their evolution. This is particularly challenging for cumuli with diameters on the order of a few hundred meters, which are common in the trade wind regime and are difficult to characterize by fast-flying research aircraft.

In section 2, a brief introduction of the CARRIBA campaign and the ACTOS payload is given. In section 3, the methods used in this study are introduced. Cloud microphysical properties, as well as an illustration of the mixing diagram with dependence on the cloud evolution, are given in section 4. This section also contains a statistical analysis of the mixing process based on mixing diagrams for clouds of different evolutionary stages. Section 5 provides a summary and the conclusions.

2. Experimental

a. The CARRIBA campaign

CARRIBA consisted of two phases, which were performed near Barbados in November 2010 and April 2011. The analysis presented here is focused on the November campaign. Characteristics of the Caribbean are the steady and uniform meteorological conditions in terms of stratification, almost constant sea surface temperature, an inversion height of approximately 3000 m, and prevailing easterly winds. All helicopter-borne measurements started with an initial profile up to approximately 2500 m followed by a number of horizontal legs in different heights under cloud-free conditions. The second half of a measurement flight was typically used to sample clouds around cloud top at relatively constant heights. However, because of changing cloud-top heights, flying at a constant height would result in a low number of sampled clouds. Therefore, the sampling altitude was adjusted, and the sampled clouds are normalized by their adiabatic value for further analysis (see section 3a). The majority of the clouds were sampled at an altitude range between 1000 and 2000 m. The cloud data were collected during horizontal flight patterns at about 100 m below the top of the cumuli. Deeper penetrations into the clouds or vertical profiling were

not possible because of flight restrictions of the helicopter. The observed shallow cumuli had an average cloud-base height of approximately 500 m. Cloud droplet diameters ranged between 5 and 40 μm on days that were characterized by relatively high aerosol conditions. On days with clean conditions, often a drizzle tail could be observed with droplet sizes up to 80 μm. Also, many of the observed size distributions showed a bimodal character. Mean cloud droplet number concentrations ranged between 70 and 135 cm^{-3}. More information about general conditions during CARRIBA can be found in Siebert et al. (2013).

b. ACTOS payload

Meteorological, turbulence, aerosol particle, and cloud microphysical parameters were sampled by instruments installed on the helicopter-borne measurement platform ACTOS (Siebert et al. 2006a, 2013). ACTOS is approximately 5 m long and has a mass of about 200 kg. It is attached to the Spectral Modular Airborne Radiation Measurement measurement system (SMART-HELIOS; Werner et al. 2013, 2014) by means of a 140-m-long rope. SMART-HELIOS, in turn, is attached to the helicopter using a 20-m-long rope. The helicopter flies with a true airspeed of about 20 m s^{-1}, which is a compromise between a stable flight position and no influence from the rotor downwash. ACTOS is an autonomous system where data are sent to the helicopter via a telemetry connection enabling online monitoring of the data. The time for a measurement flight is limited to 2 h, and the platform can be operated up to a maximum altitude of about 3000 m.

An ultrasonic anemometer (Solent HS, Gill Instruments Ltd., United Kingdom) measured the three-dimensional wind vector. The data were corrected for attitude and platform motion by means of a GPS-aided inertial navigation system. In-cloud temperature measurements were carried out with an ultrafast thermometer (UFT) with an accuracy of 0.2 K (Haman et al. 1997). The device is based on a resistance wire with a diameter of 2.5 μm. A shielding rod in front of the wire prevents droplet impacts on the sensor, which yields reliable temperature measurements within clouds (e.g., Siebert et al. 2006a). To measure absolute air humidity, an open-path infrared absorption hygrometer (LI-7500, LI-COR Inc., United States) and a dewpoint hygrometer (TP 3-S, MeteoLabor, Switzerland) were used. All instruments have a temporal resolution of at least 100 Hz, which yields a spatial resolution down to the decimeter scale. More detailed information on these instruments can be found in Siebert et al. (2006a). Measurements of cloud condensation nuclei (CCN)

were obtained using a mini-CCN counter (Roberts and Nenes 2005) operated at a supersaturation of 0.26% with an uncertainty of about 10%, which is mainly limited by the counting statistics.

For cloud microphysical measurements, a phase Doppler interferometer (PDI) was used (Chuang et al. 2008; Wendisch and Brenguier 2013). The PDI measures size and velocity of individual droplets based on the analysis of laser light scattered by the droplets. Two identical laser beams intersect and form the sample volume. A passing droplet scatters the laser light onto three spatially separated detectors. From the phase shift between the detected signals, the droplet size is derived. Also, based on the Doppler frequency shift, the velocity of the droplet is determined. The droplet sizes range from 1 to 180 μm with an uncertainty of $\pm 1 \mu$m (Chuang et al. 2008). Cloud droplet number concentration N, mean volume diameter D_v, and liquid water content (LWC) were derived from the PDI measurements using the following equations:

$$N = \frac{1}{A_p t_{\text{tot}}} \sum_i \frac{n_{c(i)}}{|v_i|}, \tag{1}$$

$$D_v = \left[\frac{\sum_i n_{c(i)} d_i^3}{\sum_i n_{c(i)}} \right]^{1/3}, \quad \text{and} \tag{2}$$

$$\text{LWC} = \frac{\pi}{6} \rho_w D_v^3 N, \tag{3}$$

where A_p is the cross section of the sample volume, t_{tot} is the integration time, $n_{c(i)}$ is the number of droplets per size bin where each bin has a width of 1 μm, $\overline{|v_i|}$ is the average absolute velocity per size bin, d_i is the mean diameter per bin, and ρ_w the density of liquid water. The droplet number concentration is corrected for size dependence of the sample volume following Chuang et al. (2008).

3. Methods

a. Estimating adiabatic cloud properties

At cloud base, a certain number of aerosol particles will be activated to cloud droplets. During adiabatic lifting of the cloudy air parcel, no further activation occurs, and the droplet number concentration remains constant at its adiabatic value N_{ad}.

Because no measurements with ACTOS at cloud base are available, N_{ad} will be estimated from CCN observations in the subcloud layer (SCL), which is assumed to be well mixed. Here, the 95th percentile of CCN concentration measured in the SCL is used because, as

shown by Ditas (2014), the prevailing supersaturation was often larger than the supersaturation used for the mini-CCN counter. Although Topping et al. (2013) showed that using CCN concentration as a proxy for N_{ad} might result in an underestimation, at the moment there is no better way to estimate the adiabatic droplet concentration.

LWC will increase nearly linearly during the lifting of the cloudy air parcel, and the adiabatic LWC can be calculated using the first law of thermodynamics:

$$\text{LWC}_{ad}(z) = \frac{c_p}{L} \int_{z_{cb}}^{z} \rho(z') \left(\frac{g}{c_p} + \frac{dT}{dz'} \right) dz', \quad (4)$$

where z_{cb} is the height of cloud base, ρ is the density of air, g is the acceleration due to gravity, $L = 2.5 \times 10^6 \, \text{J kg}^{-1}$ is the latent heat of vaporization, $c_p = 1004 \, \text{J kg}^{-1} \text{K}^{-1}$ is the specific heat capacity of air at constant pressure, and dT/dz' is the wet adiabatic lapse rate. For a given z_{cb} with temperature T_0, Eq. (4) can be solved numerically for any height z. With N_{ad} and LWC_{ad}, the adiabatic mean volume diameter is obtained by

$$D_{v,ad} = \left(\frac{6}{\pi \rho_w} \frac{\text{LWC}_{ad}}{N_{ad}} \right)^{1/3}. \quad (5)$$

$D_{v,ad}$ is also an increasing function with increasing height.

Clouds experience turbulent entrainment and mixing; therefore, observed cloud microphysical parameters may deviate from their adiabatic values. To compare clouds sampled under different conditions, the actual measured parameter $\zeta(x_i, t)$, with ζ being a cloud parameter such as LWC, N, or D_v, is normalized by its adiabatic value:

$$\zeta_n = \zeta/\zeta_{ad}. \quad (6)$$

To calculate LWC_{ad}, the cloud-base height has to be estimated. From constant low-level flights at the height z over the sea, the mean temperature $T(z)$ and dewpoint temperature $T_D(z)$ are derived with an estimated accuracy of 0.2 K for both parameters. With the known lapse rates dT/dz and dT_D/dz, the height where $T(z_{cb}) = T_D(z_{cb})$ can be calculated:

$$z_{cb} = \frac{T(z_s) - T_D(z_s)}{dT_D/dz - dT/dz}, \quad (7)$$

where z_s is the sea surface height. With an adiabatic dry lapse rate of $dT/dz = -g/c_p = -9.8 \, \text{K} \, (1000 \, \text{m})^{-1}$ and a mean observed lapse rate for the dewpoint of $-1.8 \, \text{K}$ $(1000 \, \text{m})^{-1}$, we obtain $z_{cb} = [T(z_s) - T_D(z_s)] \times 125 \, \text{m K}^{-1}$

(also known as the Henning equation). The measurement of the spread $T(z_s) - T_D(z_s)$ includes an absolute error of 0.4 K. The error of cloud-base estimation is about 50 m, assuming errors in the lapse rates can be neglected. Estimated cloud-base heights were supported by ceilometer data obtained from the Barbados Cloud Observatory (e.g., Nuijens et al. 2014).

As a next step, we estimate the error of LWC_{ad} resulting from an error of 50 m in cloud-base estimation. For simplicity, we estimate this error for only one selected measurement height of 1.5 km, which is a typical height for our cloud observations. With $z_{cb} = 500 \, \text{m}$ and $T(z_{cb}) = 24°\text{C}$, we find $\text{LWC}_{ad} = 2.3 \, \text{g m}^{-3}$ and for $z_{cb} = 550 \, \text{m}$, $\text{LWC}_{ad} = 2.2 \, \text{g m}^{-3}$; that is, the absolute error is $\Delta \text{LWC}_{ad} \approx 0.1 \, \text{g m}^{-3}$ for this observation height. A small difference of $\Delta T(z_{cb}) = 0.5 \, \text{K}$ for the two different cloud-base heights has a negligible effect on LWC_{ad}.

Finally, we estimate the absolute error for $D_{v,ad}$ based on the observation example: with $\text{LWC}_{ad} = 2.2 \, \text{g m}^{-3}$ and a typical value of $N_{ad} = 100 \, \text{cm}^{-3}$, we find:

$$\Delta D_{v,ad} = \frac{1}{3} \left(\frac{6}{\pi \rho_w N_{ad}} \right)^{1/3} (\text{LWC}_{ad})^{-2/3} \Delta \text{LWC}_{ad} \approx 0.5 \, \mu\text{m}. \quad (8)$$

Next, we consider the absolute error of estimated N_{ad}. Ditas (2014) compared measured CCN at a supersaturation of 0.26% with measured activated particles [see, e.g., Fig. 4.12b in Ditas (2014)]. Both number concentrations differ by about 20%, which we consider as the error for N_{ad}. Therefore, we find the following:

$$\Delta D_{v,ad} = \frac{1}{3} \left(\frac{6 \text{LWC}_{ad}}{\pi \rho_w} \right)^{1/3} (N_{ad})^{-4/3} \Delta N_{ad} \approx 2.3 \, \mu\text{m}. \quad (9)$$

This discussion of the accuracy of the measurements is important for the following analysis of the mixing diagrams.

b. Classification of shallow cumuli with respect to evolution stage

A typical feature of the trade wind area is the concurrent presence of clouds at different stages of evolution. Actively growing clouds can be observed next to dissolving ones. This is caused by the permanent triggering of development of shallow cumuli under almost-constant thermodynamic and dynamic conditions. The three cloud life cycle stages (actively growing, decelerated, and dissolving) following Katzwinkel et al. (2014) are defined by the 90th percentiles of vertical wind velocity w and buoyancy acceleration B in the cloud interior. As in Katzwinkel et al. (2014), the cloud

interior is defined as the region with LWC > 0.2 g m^{-3}. The actively growing clouds are characterized by positive buoyancy and updrafts ($B > 0$ and $w > 0$). The decelerated clouds are negatively buoyant but still exhibit an updraft ($B < 0$ and $w > 0$). The dissolving clouds reveal negative buoyant cloud interiors with downdrafts ($B < 0$ and $w < 0$).

This classification is based on the measured vertical velocity and the calculated buoyancy $B = g \times (\theta_v - \overline{\theta}_v)/\overline{\theta}_v$, where $\theta_v = \theta(1 + 0.61 q_t - 1.61 q_l)$ is the virtual potential temperature, q_t and q_l are the total and liquid water mass mixing ratios, and the overbar denotes the cloud-free environmental mean value calculated for each cloud individually. Closely following the principles made by Katzwinkel et al. (2014), only clouds fulfilling the following criteria were analyzed: the cloud interior region has to have a diameter of at least 20 m, and the distance between one cloud and its neighbor has to be at least 60 m to avoid cloud edges being affected by other clouds. Even though we follow the method used by Katzwinkel et al. (2014), we decreased the distance between two clouds from 100 to 60 m to increase the number of dissolving clouds for our analysis. Generally, a cloud is defined to be present when LWC > 0.02 g m^{-3}.

A total of 177 active, 91 decelerated, and 32 dissolving clouds were classified. The disproportion results from the flight strategy aiming at well-developed shallow cumuli, as well as from the strict criteria for individual clouds. Some of the dissolving clouds might have too-low LWC or might be too narrow in diameter. The analysis of this work focuses mainly on the actively growing and the dissolving clouds, as the decelerated cloud stage can be seen as an intermediate state between these two cloud stages.

The classification has some limits because of the fact that most of the measurements are performed about 100 m below cloud top. It might occur that the top of an actively growing cloud was sampled, but this region might belong to an overturning eddy, and therefore the cloud would be falsely classified as a dissolving cloud.

c. The mixing diagram

Jensen et al. (1985) analyzed the dependence of the droplet concentration N on the fraction of cloud-base air F in a sample of cloudy air. Based on this N–F diagram, Burnet and Brenguier (2007) defined a mixing diagram that illustrates the LWC as a function of cloud droplet number and volume: LWC $\propto ND_v^3$ [see Eq. (3)]. Plotted are droplet number concentrations N_n versus cubed mean volume diameters $D_{v,n}^3$ where the subscript n denotes normalization by the respective adiabatic values [see Eq. (6)]. An example for such a diagram is given in Fig. 1 by Lehmann et al. (2009). The mixing diagrams

contain isolines for homogeneous mixing (saturation lines), which represent the change in the $[N_n; D_{v,n}^3]$ values if entrainment and mixing of environmental air with a certain subsaturation takes place and all droplets are assumed to respond uniformly. Data points falling on the saturation lines indicate that the mixing process is homogeneous. The droplet size distribution is shifted toward smaller diameters, and N is reduced because of dilution. Also, data points located to the right of the saturation line for the environmental relative humidity (RH) cannot be physically explained by mixing. In the case of inhomogeneous mixing, data points lie on a horizontal line. Consequently, no shift of the size distribution is observed; only a reduction of the cloud droplet number occurs, as a subset of the droplets evaporates completely. As additional information, the mixing fraction similar to Kain and Fritsch (1990),

$$\chi = (q_t - \max[q_{t,c}])/(\overline{q}_{t,e} - \max[q_{t,c}]), \qquad (10)$$

which describes the fraction of entrained air, is included in the mixing diagrams. Here, q_t is the total water mixing ratio, the subscripts e and c denote the environmental and cloud values, and the overbar marks the mean value. For nonadiabatic conditions, χ is a measure of the relative dilution of cloud regions with respect to the maximum observed total water mixing ratio within the respective cloud.

d. Statistical mixing analysis

To classify the mixing process of all considered clouds, two methods are applied. The first is based on the mixing diagrams described in the previous subsection. The spread in the droplet size $\Delta D_{v,n}^3$, which is defined as the difference between the maximum and the minimum value of $D_{v,n}^3$ for a single cloud, is determined for each diagram individually. Large $\Delta D_{v,n}^3$ values are taken as an indicator for homogeneous mixing, whereas small values represent inhomogeneous mixing.

As another strategy, a D_v susceptibility α is defined based on the principles introduced by Feingold et al. (2001). This quantity describes the relative change in $D_{v,n}^3$ related to the relative change in N_n and is given by the following:

$$\alpha = \frac{\Delta D_{v,n}^3/D_{v,n}^3}{\Delta N_n/N_n} = \frac{\Delta D_{v,n}^3}{\Delta N_n}\frac{N_n}{D_{v,n}^3} = \frac{d\ln D_{v,n}^3}{d\ln N_n}. \qquad (11)$$

To estimate a theoretical maximum value of the D_v susceptibility $\alpha_{\max}$, we consider a homogeneous mixing line for RH = 83%, which is the 10th percentile of the observed RH in the close vicinity (20-m distance from cloud edge) of all analyzed clouds. In a log–log diagram
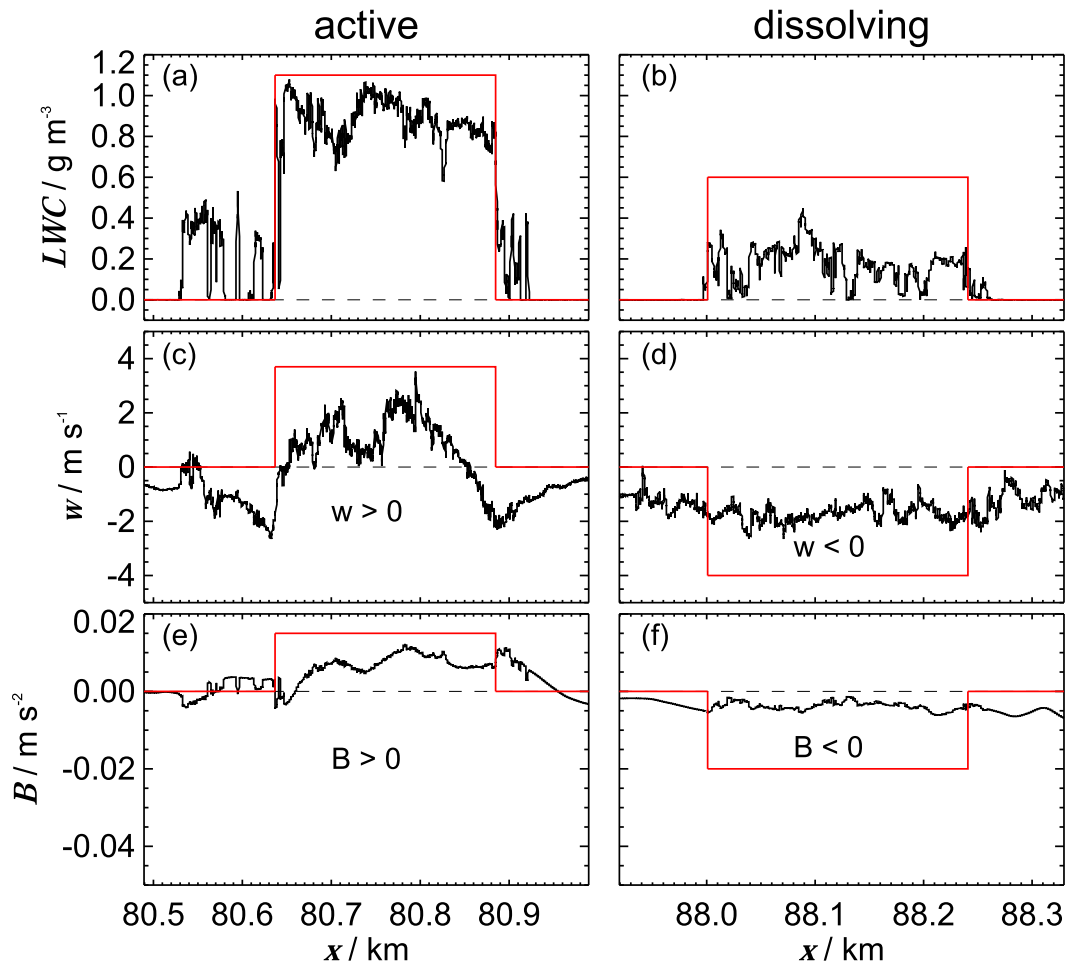
FIG. 1. Horizontal cross section through single clouds showing (a),(b) liquid water content; (c),(d) vertical velocity; and (e),(f) buoyancy for actively growing and dissolving clouds. Red lines mark the cloud interior region, and x is the horizontal distance during the helicopter flight.

the homogeneous mixing line is fitted linearly in the range of $0.7 < D_{v,n}^3 < 1$ to take into account the non-linear character of these homogeneous mixing lines. The slope of this fit represents the theoretical maximum value, with $\alpha_{max} = 1.66$. Therefore, $\alpha = 1.66$ indicates perfectly homogeneous mixing, whereas $\alpha = 0$ corresponds to perfectly inhomogeneous mixing.

4. Data analysis

a. Cloud stage classification

In Fig. 1, examples are given for clouds from the actively growing and the dissolving cloud stage. The red lines indicate the cloud interior (LWC $> 0.2\,\mathrm{g\,m^{-3}}$). Figures 1a and 1b show time series (distance) of LWC for each cloud. The actively growing cloud reveals large values of LWC with mean values of approximately $1\,\mathrm{g\,m^{-3}}$, whereas the dissolving cloud shows low values

of LWC $\approx 0.3\,\mathrm{g\,m^{-3}}$. The edges of the clouds are characterized by low LWC because of the definition of cloud edges, and they vary in extent. In Figs. 1c and 1d the time series of w are shown for each cloud type. The active cloud has an updraft in the interior region with maximum values of about $3\,\mathrm{m\,s^{-1}}$. The dissolving cloud has negative vertical velocities of about $-2\,\mathrm{m\,s^{-1}}$ in its interior. Time series of B are shown in Figs. 1e and 1f, with the actively growing cloud being positively buoyant with maximum values around $0.01\,\mathrm{m\,s^{-2}}$, whereas the dissolving cloud is negatively buoyant with a mean of $B \approx -0.005\,\mathrm{m\,s^{-2}}$ in the interior.

In Fig. 2, the statistics of the 90th percentiles of w and B in the cloud interior region are shown for all classified clouds. Each box represents 50% of the data and indicates the median value by a horizontal line. Whiskers denote the 12.5th and 87.5th percentiles and, thus, represent 75% of the data. Actively growing clouds have
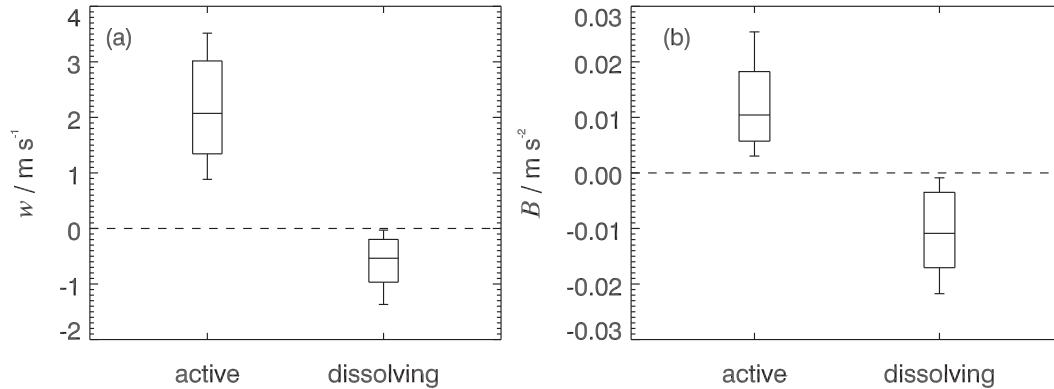
FIG. 2. Box-and-whisker plots of 90th percentile of (a) vertical wind velocity and (b) buoyancy acceleration. The box represents, as in all box-and-whisker plots in this work, 50% of the data and contains the median value. The whiskers mark the 12.5th and 87.5th percentile, thus representing 75% of the data.

high vertical velocities with a median value of about $2\,\mathrm{m\,s}^{-1}$. They also show a large spread in w where 50% of the data lie in a range of approximately $1.3–3.1\,\mathrm{m\,s}^{-1}$. The dissolving clouds are characterized by a median w of around $-0.5\,\mathrm{m\,s}^{-1}$ and a small spread where 50% of the data are in a range from -0.2 to $-0.8\,\mathrm{m\,s}^{-1}$.

Buoyancy acceleration is positive for the active clouds with a median value of $B \approx 0.01\,\mathrm{m\,s}^{-2}$. The dissolving stage shows median values of about $-0.01\,\mathrm{m\,s}^{-2}$. Both cloud stages show a comparable spread.

b. Cloud microphysical properties

Figure 3 shows the variability of N_n, LWC_n, and $D_{v,n}$ integrated over 1 s, (approximately 20 m) from all observed clouds. Especially for N_n (Fig. 3a) and LWC_n (Fig. 3c), large differences are obvious for both the different cloud regions and different cloud stages. LWC_n is smaller for the edges (gray shaded boxes) compared to the interior (white boxes) of the clouds, as expected from the definition of cloud interior ($\mathrm{LWC} > 0.2\,\mathrm{g\,m}^{-3}$). Also, for the cloud interior, some observations of $\mathrm{LWC} < 0.2\,\mathrm{g\,m}^{-3}$ were made, especially for the dissolving clouds. This is a result of the inhomogeneities [e.g., cloud holes, see Werner et al. (2013)] connected to shallow cumuli, which can result in a large variability in LWC, even close to the cloud-core region. In our analysis, we only include clouds where periods with significant dips in LWC are shorter than 2 s.

The behavior of LWC_n reflects especially in N_n, which has a median value that is more than twice as large for the interior compared to the edges of the clouds because of the continuous entrainment of subsaturated air. The spread in both parameters is larger for the interior regions compared to the edges. Also, for the dissolving stage, the median values of N_n and LWC_n decrease to approximately half of the value observed for the active stage for both the interior and the edges.

These findings can already be used to get a first idea of the mixing processes occurring in these clouds: Burnet and Brenguier (2007) analyzed data from the Small Cumulus Microphysics Study (SCMS) experiment and found that these clouds showed features of both homogeneous and inhomogeneous mixing. They observed homogeneous mixing when the cloud LWC was slightly diluted and inhomogeneous mixing when the LWC was more diluted. Therefore, it is likely that the dissolving clouds mix rather inhomogeneously, whereas the actively growing clouds tend to mix more homogeneously.

The differences in $D_{v,n}$ for the two stages, shown in Fig. 3b, are comparably small. For the cloud interior, the median of $D_{v,n}$ shows a small decrease from 0.83 for active clouds to 0.77 for dissolving clouds. The same holds true for the cloud edges, which show a slight decrease from 0.76 to 0.73. It appears that $D_{v,n}$ stays almost constant for cloud interior and cloud edge as well as for the transition from the active to the dissolving stages. This leads to the assumption that, during the transition from the active to the dissolving stages, the droplet size does not change significantly, and the reduction in LWC, as observed in Fig. 3c, is mainly due to a reduction in droplet number. This indicates that dissolving clouds might tend to mix rather inhomogeneously, as the described feature represents the characteristics of inhomogeneous mixing (e.g., Jensen et al. 1985).

In Fig. 3 the mean droplet size is analyzed by using height-independent normalized values. As a next step, the droplet size distribution is investigated for the active and dissolving cloud stages by looking at the mean droplet size $\overline{D}$, the spectral width σ, which is the standard deviation of the size distribution, and the spectral dispersion $\sigma/\overline{D}$. Both parameters are a function of height (e.g., Warner 1969). This analysis is motivated by the hypothesis that the mixing process may cause a broadening of the size distribution (e.g., Warner 1969; Telford
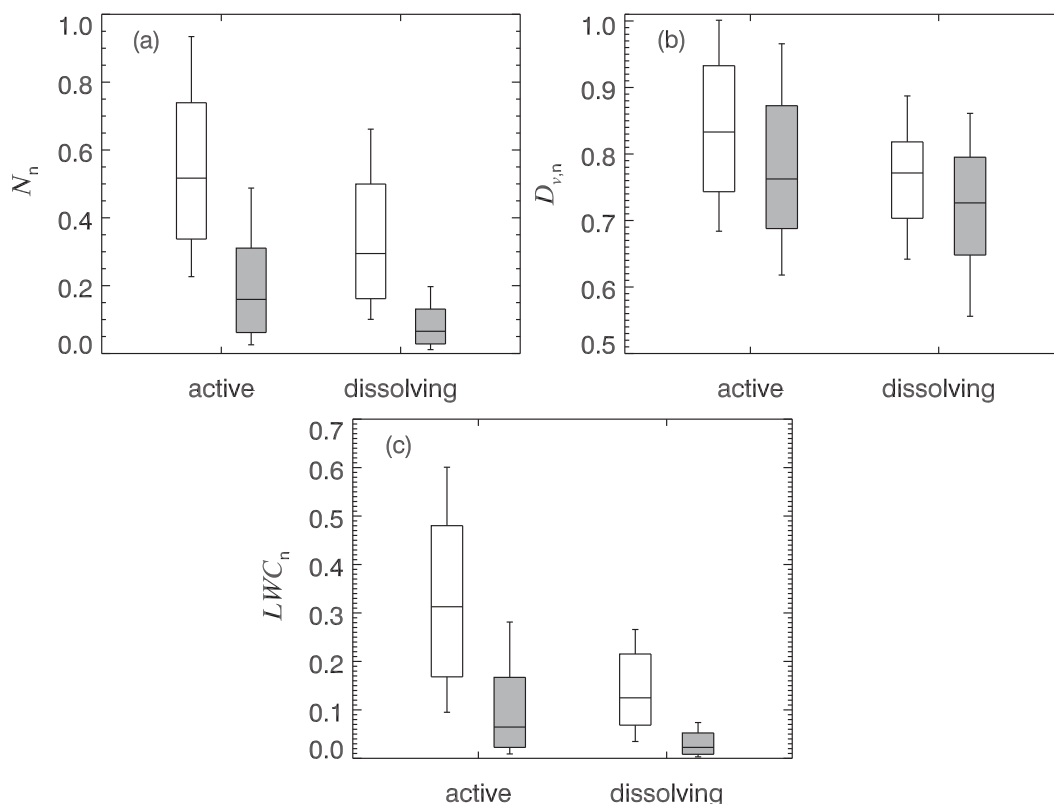
FIG. 3. Box-and-whisker plots of (a) normalized cloud droplet number concentration, (b) normalized mean volume diameter, and (c) normalized liquid water content for actively growing and dissolving clouds. Open boxes represent cloud-interior data, and gray-shaded boxes represent cloud-edge data.

and Chai 1980; Baker et al. 1980; Su et al. 1998; Burnet and Brenguier 2007). Therefore, we focus again on the actively growing and the dissolving stage of evolution. Figure 4a shows the profile of $\overline{D}$; each data point represents the mean droplet size for the respective height interval of 200 m to account for the increase in droplet size with increasing altitude. For the height range between 1000 and 1800 m, an increase in $\overline{D}$ is observed for both cloud stages. Above this altitude a slight decrease in the mean droplet size is found. For the altitude of 2400 m, a smaller number of cloud droplets was detected, which makes these data points statistically less significant compared to the ones for lower altitudes. Active clouds have larger $\overline{D}$ throughout the entire profile with a mean difference between the two stages of about 2.3 μm. Figure 4b shows the profile of σ for the two stages. At the lowest observation heights, σ is about 4 μm, whereas at the highest altitude, σ is approximately 8 μm. Such an almost-linear increase of σ with increasing altitude is similar to observations (e.g., Arabas et al. 2009). The linear fit for both cloud stages is nearly identical, which indicates that the difference in σ between the two stages is minor. Therefore, it is concluded that the observed droplet size distributions broaden with

height, and there is no significant difference for active and dissolving clouds. In Fig. 4c, a profile of the mean spectral dispersion is shown for the active and dissolving clouds. An increase with height can be observed, especially for the dissolving clouds.

When analyzing the cloud droplet size distribution of the observed clouds, three different types of size distributions could be found. Some clouds showed monomodal distributions with only one distinct peak at small droplet sizes in the range between 10 and 20 μm. Other clouds showed a bimodal structure in their droplet size distributions, with a small mode peaking at about 10 μm. To measure the significance of the individual modes, Gaussian fits are applied, and the absolute number of droplets X_i of the ith mode with the size range $\mu_{d,i} \pm \sigma_{d,i}$ is calculated. Here, $\mu_{d,i}$ is the mean and $\sigma_{d,i}$ is the standard deviation of the Gaussian fit. The value X_1 is the number of droplets in the small mode, and X_2 is the number of droplets in the main mode. This small mode might be an indication for secondary activation (Warner 1969), which has the potential to significantly increase the total droplet number concentration and has to be considered in the upcoming analysis. Therefore, a threshold of $X_1/X_2 < 0.5$ is introduced, where
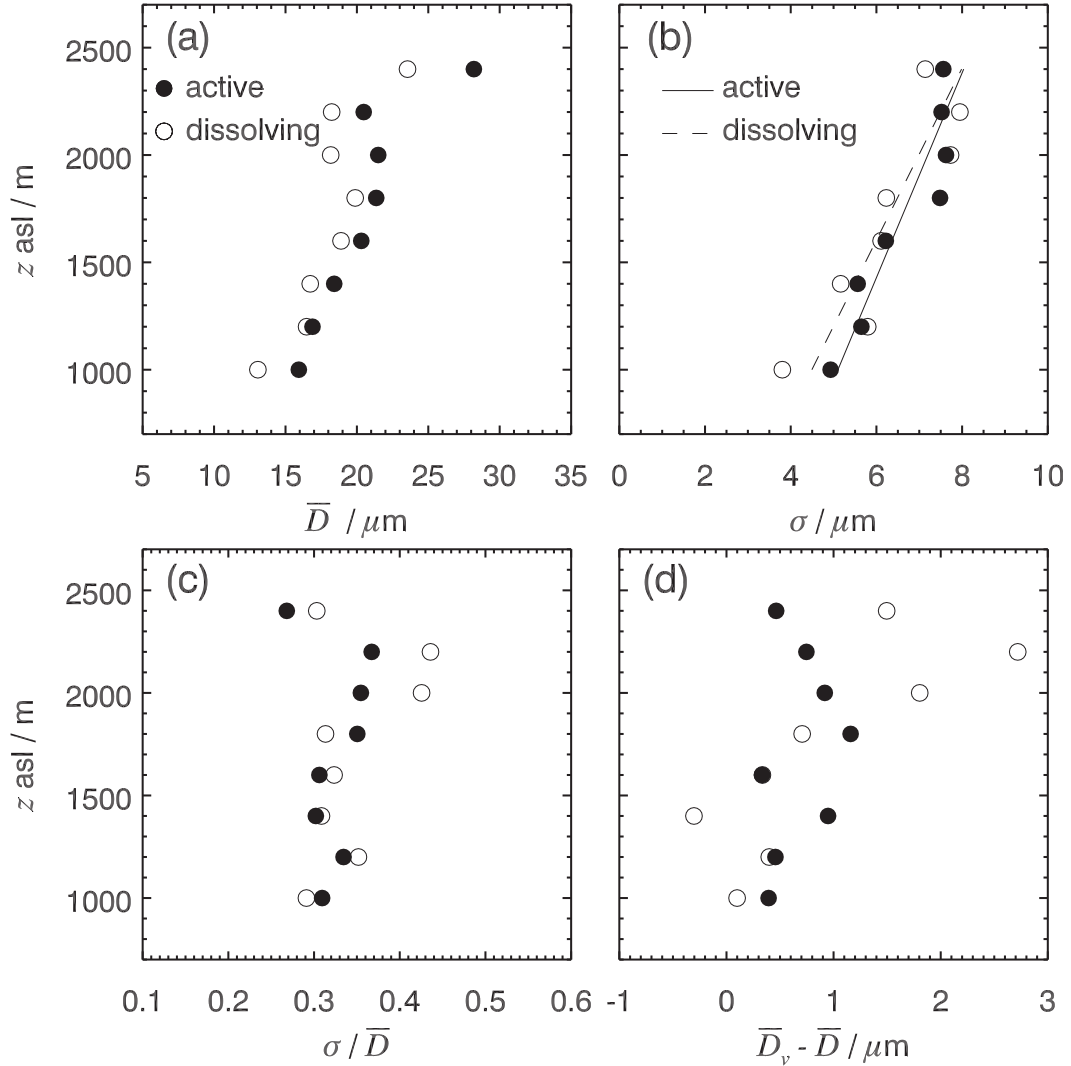
FIG. 4. Profile of (a) mean droplet diameter, (b) mean spectral width, (c) spectral dispersion, and (d) the difference between $\overline{D_v}$ and $\overline{D}$ for actively growing (full circles) and dissolving (open circles) clouds. Solid and dashed lines represent linear fits. No separation between cloud-interior and cloud-edge regions is applied.

secondary activation is considered to be nonsignificant for the following analysis in sections 4c and 4d. For $X_1/X_2 > 0.5$ the impact of secondary activation is considered to be significant. An example of the three types of droplet size distributions is given in Fig. 5. From the 300 observed clouds, 9% show pure monomodal distributions, 45% show bimodal distributions with no significant impact from secondary activation, and 46% show bimodal distributions where secondary activation is significant. A more detailed discussion of the subject of secondary activation is given in section 5a.

c. Mixing diagram analysis

An example of a mixing diagram is shown in Fig. 6 for the actively growing and the dissolving cloud stages,

where each diagram contains data from one individual cloud. The colors indicate the mixing fraction χ of entrained air, with $0 < \chi < 0.33$ in red, $0.33 < \chi < 0.66$ in green, and $0.66 < \chi < 1$ in blue. The open circles represent data obtained from the edge region of the cloud, whereas solid circles are derived from the cloud interior. Each data point is derived by integrating over 1 s of cloud microphysical data. Solid curved lines, as well as the horizontal line where the cubed normalized mean volume diameter $D_{v,n}^3 = 1$, represent homogeneous mixing lines for environmental air with a certain subsaturation given in percentages of RH. The thick line represents the actual environmental RH.

Figures 6a–c show three examples of actively growing clouds, which are not significantly affected by secondary
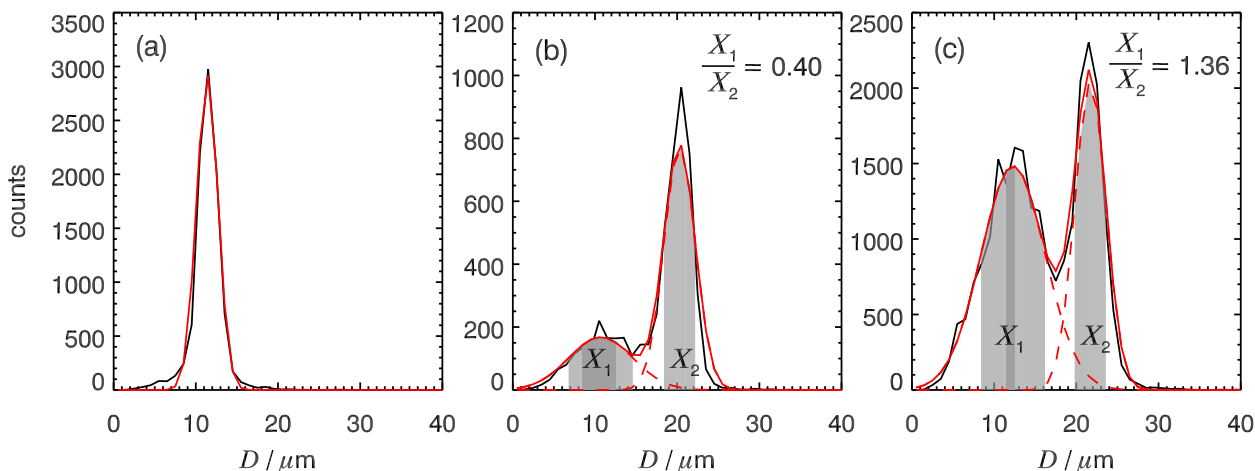
FIG. 5. Example of cloud droplet size distributions for (a) a monomodal distribution, (b) a bimodal distribution with nonsignificant contribution of droplets formed by secondary activation, and (c) a bimodal distribution with a significant small mode formed by secondary activation. The solid red lines represent the fitted distribution, and the dashed red lines represent the individual modes. The ratio of the number of droplets in the small mode to the number of droplets in the main mode is given for the bimodal distributions.

activation, according to our definition (section 4b). Figures 6a and 6b show a clustering of data points around the saturation line for 99% RH, indicating homogeneous mixing, but at a higher RH than the environment (RH = 80%). Data points with small χ are derived from the interior of the cloud and also show the largest values of N_n and $D_{v,n}^3$. Data points from the cloud edges show larger χ values, indicating that, because of mixing, the fraction of entrained air is between 67% and 100% relative to the maximum observed $q_{t,c}$. The cloud represented by Fig. 6c also seems to have undergone homogeneous mixing, even though the data points are not directly placed on one homogeneous mixing line but are clustered between the lines of 90% and 99% RH. Based on section 3a, an absolute error of $\Delta N_n \approx 0.2$ and $\Delta D_{v,n}^3 \approx 0.2$ is estimated. It should be noted that this error is the same for all data points in the diagram. Therefore, the data ensemble would only be shifted, but the structure remains the same. This can explain why the red data points in Fig. 6c are located slightly to the right of the thick saturation line (but cannot explain the points lying to the right of the thick saturation line in Figs. 6d and 6e, as discussed below). Again, data points with the largest values of N_n and $D_{v,n}^3$ have the smallest χ values, whereas data that deviate the most from adiabatic conditions have the largest χ values. For all three active clouds, the $D_{v,n}^3$ values derived from the cloud interior decrease from almost 1 to about 0.6 (Figs. 6a,b) and 0.4 (Fig. 6c). Cloud-edge data show even lower normalized diameters down to 0.2. The normalized cloud droplet number concentration is mostly larger for the interior than for the edges. The value of N_n ranges from 0.2 to 0.7 (Figs. 6a,b) and even up to 1.0 (Fig. 6c) for

the interior and reaches maximum values of 0.6 (Fig. 6c) for the cloud edge.

Figures 6d–f show mixing diagrams for dissolving clouds, where data points with the lowest χ belong to the largest N_n, even though for the droplet size only relatively low normalized values are observed. The diagrams show points located horizontally at $D_{v,n}^3$ of about 0.5 (Figs. 6d,f) and about 0.3 (Fig. 6e). An error in $D_{v,ad}$ due to $\Delta N_{ad} = 20\%$ (see discussion in section 3a) can only explain a horizontal displacement of approximately 10%. Therefore, the observed horizontal distribution at $D_{v,n}^3 \approx 0.5$ or lower is not attributed to measurement uncertainties. Also remarkable are the high normalized number concentrations observed in Figs. 6d and 6e, which are close to adiabatic conditions. The position of data points to the right of the saturation line corresponding to the environmental relative humidity cannot be explained by mixing alone. Both clouds have droplet size distributions with a significant small mode; therefore, secondary activation, which acts as a local droplet source, is most likely the cause of the high N_n values to the right of the thick saturation line. Also, the derivation of the horizontally distributed data points from $D_{v,n}^3 = 1$ could be explained by this mechanism. For all three dissolving clouds, the data points observed from the edge of the clouds correspond to low N_n values, whereas the interior data shows larger normalized number concentrations. The cloud shown in Fig. 6f is not significantly affected by secondary activation. This cloud shows mostly low χ values in the interior, which implies that this cloud region is uniformly diluted with respect to the maximum observed $q_{t,c}$. Also, it is assumed that $\max[q_{t,c}]$ deviates significantly from the adiabatic value of $q_{t,c}$.
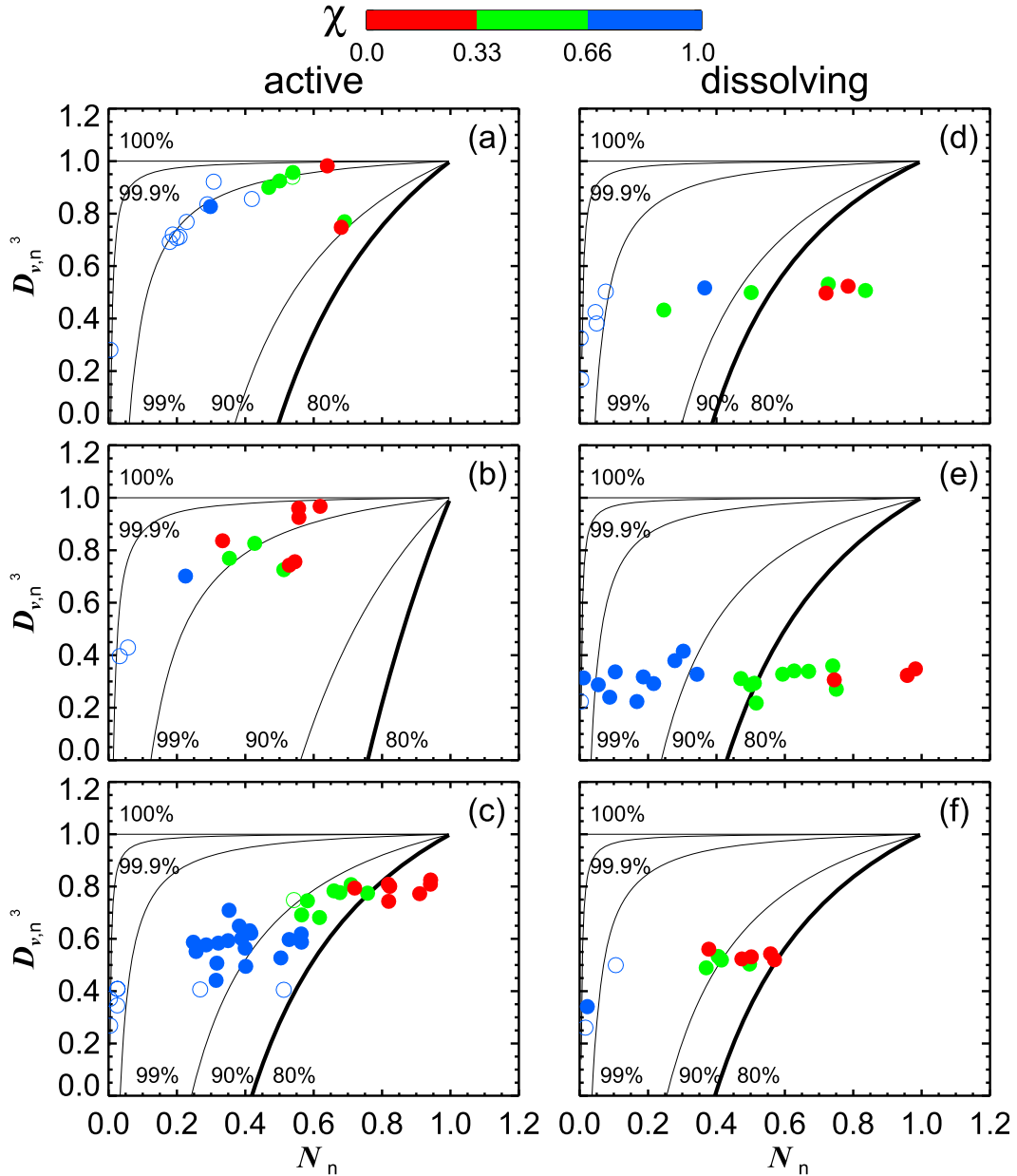
FIG. 6. Mixing diagrams of (a)–(c) actively growing clouds and (d)–(f) dissolving clouds. Solid lines starting at [1, 1] represent the variation of $D_{v,n}^3$ and N_n during homogeneous mixing of entrained air with different saturation values (given in percentage of RH). The thick line represents the actual environmental RH. The color code indicates the fraction of entrained air. Open circles represent data points obtained from the edge regions of the clouds, whereas solid circles are derived from the cloud interior.

Based on Fig. 6, the hypothesis is made that there is a trend for a transition from homogeneous toward inhomogeneous mixing as the clouds evolve from the actively growing to the dissipating stage. In actively growing clouds the droplet size and droplet number concentration decrease as a result of homogeneous mixing. When the cloud reaches the dissipating stage, the droplet size deviates significantly from its adiabatic value because of the reduction in size when the cloud was still at the actively growing stage. Because of inhomogeneous mixing, the cloud droplet size remains then rather constant, but the droplet number concentration decreases strongly in the dissolving clouds, and the data points are located almost horizontally at lower values of $D_{v,n}^3$. The diagrams for the dissolving stage closely resemble the mixing diagram of case III (Fig. 5c)
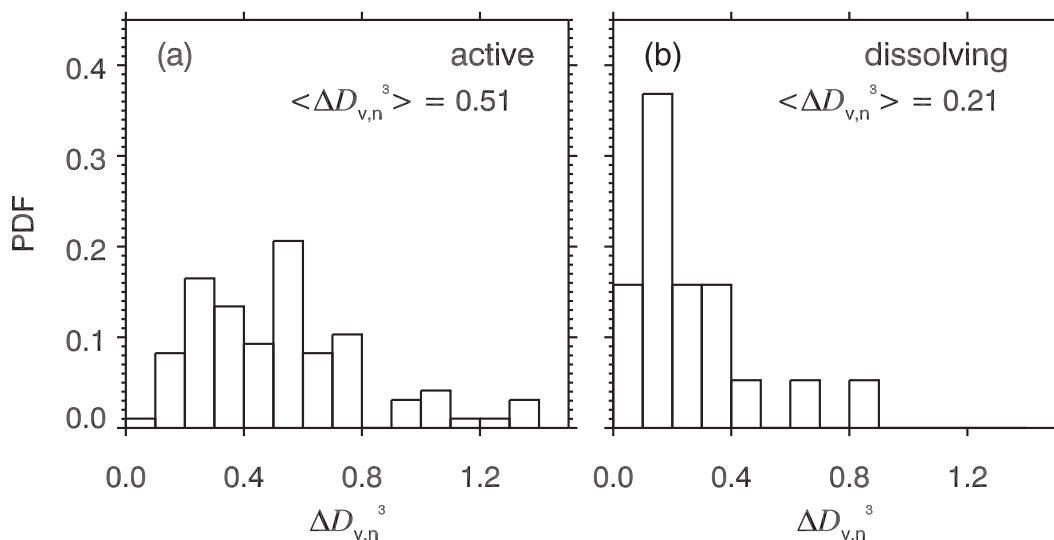
FIG. 7. PDF of the spread in droplet mean volume diameter for (a) actively growing clouds and (b) dissolving clouds, which show no signs of significant secondary activation. The median value is given in each panel.

from Lehmann et al. (2009), which shows inhomogeneous mixing in a dissipating cloud.

d. Statistical mixing analysis

The spread in the cubed droplet size $\Delta D_{v,n}^3$ is calculated for all individual clouds based on the respective mixing diagrams where no discrimination between cloud edge and interior data is applied. Figure 7 shows the probability density function (PDF) of $\Delta D_{v,n}^3$ for clouds showing no signs of significant secondary activation. The actively growing clouds cover a wide distribution of $\Delta D_{v,n}^3$ values ranging up to 1.4. The dissolving stage shows a comparably narrow distribution, with $\Delta D_{v,n}^3$ values ranging up to 0.9. Also, the dissolving stage shows a large probability for $\Delta D_{v,n}^3$ values below 0.4 when compared to the actively growing stage. This is reflected in the median values of $\Delta D_{v,n}^3$, which are 0.51 for active clouds and 0.21 for the dissolving stage. The larger spread for the actively growing clouds indicates a trend toward homogeneous mixing, whereas the smaller spread for the dissolving clouds supports the finding of the mixing diagrams of inhomogeneous mixing. The same analysis is done for clouds that are significantly affected by secondary activation. The results are not shown here, as they show no significant difference between the cloud evolutionary stages with median values of 0.37 for the actively growing clouds and 0.31 for the dissolving clouds.

In Fig. 8, the analysis of the D_v susceptibility α is performed using a log–log diagram. For each cloud stage, the median value of $\ln(D_{v,n}^3)$ in bins of $\ln(N_n)$ is calculated and plotted. Bars denoting the 25th and 75th percentile of $D_{v,n}^3$ are given for each bin. The data are

fitted linearly, and the slope represents α for the respective cloud stage. The value of α is analyzed for both clouds showing purely monomodal droplet size distributions (Figs. 8a,b) and clouds showing significant secondary activation (Figs. 8c,d). No distinction between cloud interior and edge has been made.

The actively growing clouds with purely monomodal size distributions show a relatively large D_v-susceptibility value of $\alpha = 0.21$, whereas for the dissolving clouds with purely monomodal distributions, $\alpha = 0.0$ is obtained. Regarding clouds showing significant signs of secondary activation, no difference in α is found, as for both cloud stages $\alpha = 0.03$ is obtained. The relatively low correlation coefficients R are due to the rather low number of observed clouds.

To summarize, we found that when only taking into account clouds with purely monomodal droplet size distributions, the actively growing clouds have a larger decrease in diameter as the number concentration decreases compared with the dissolving clouds. It is concluded that the homogeneity of mixing decreases with cloud stage from active to dissolving, even if actively growing clouds are not close to pure homogeneous mixing (i.e., $\alpha \approx 1.66$). Also, part of the deviation from perfect homogeneity may likely be due to more complicated factors, such as secondary activation, which tend to mask the signature of homogeneity.

5. Discussion

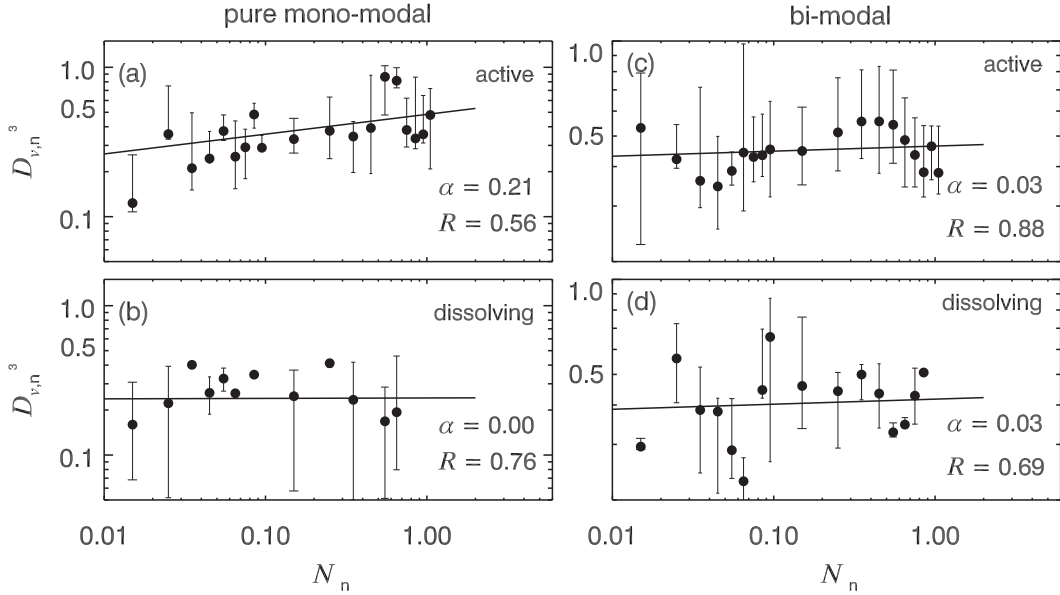The mixing diagrams presented in section 4 show features that cannot be explained using the theory of

FIG. 8. D_v susceptibility α showing the relative changes in $D_{v,n}^3$ vs relative changes in N_n for (a),(b) clouds with purely monomodal size distributions and (c),(d) clouds showing significant signs of secondary activation. Data are derived from (a),(c) actively growing clouds and (b),(d) dissolving clouds. The solid line represents a linear fit, and its slope α is given in each panel. Also, the correlation coefficient R between the fit and the data points is given. Bars denote the 25th and 75th percentile of $D_{v,n}^3$ for each data point.

homogeneous and inhomogeneous mixing. The existence of data points with relatively constant $D_{v,n}^3 < 1$ but high N_n of approximately 1 (cf. Fig. 6e, for example) needs to be discussed. These high values of N_n are sometimes even above the mixing line for the lowest relative humidity (thick mixing line in Fig. 6). That is, sources other than mixing have to be considered to explain the high values of N_n. Secondary activation, which has the potential to produce a large number of small droplets, is most likely the process behind these findings. Moreover, as already discussed in section 4b, 46% of the observed clouds have droplet size distributions that show signs of significant secondary activation. Therefore, this process is discussed in section 5a as one explanation. Also, the strong reduction of N_n and LWC$_n$ at almost-constant values of $D_{v,n}$ during the transition from the active to the dissolving stage indicates dilution that might be a result of entraining almost saturated but droplet-free air into the cloud, which motivates an investigation of possible humidity shells around the clouds (section 5b).

a. Secondary activation

Secondary activation of CCN is a well-known process that can explain a significant proportion of small droplets that is sometimes observed at higher altitudes than the cloud base (Baker and Latham 1979; Paluch and Knight 1984; Austin et al. 1985; Hill and Choularton

1985; Stith and Politovich 1989; Paluch and Baumgardner 1989; Pontikis and Hicks 1993; Brenguier and Chaumat 2001). Also, in large-eddy simulation (LES) studies, this phenomenon was observed to produce small droplets in the mixing zone well above cloud base (Slawinska et al. 2012). The occurrence of secondary activation seems a plausible explanation because of the weak condensational sinks due to low cloud droplet number concentrations of 100–200 cm^{-3} observed during CARRIBA. There are different possible mechanisms to obtain $[N_n; D_{v,n}^3]$ data, as presented in Fig. 6g, and at least 48 other clouds for which the mixing diagrams are not explicitly shown here.

For the discussion of secondary activation, the evolution of supersaturation, described by $dS/dt = a_0 w - bN(\overline{D}/2)S$, is the controlling factor. Here, S is the supersaturation, and a_0 and b are thermodynamic coefficients. Also, in liquid water clouds the quasi-steady supersaturation $S_{qs} = a_0 w / [bN(\overline{D}/2)]$ defines the equilibrium supersaturation, which is reached when an increase (decrease) in RH is balanced by the depletion (release) of water vapor by cloud droplets (Cooper 1989; Rogers and Yau 1989; Korolev and Mazin 2003). Droplet size and number, as well as w, determine the amount of S. Therefore, it is essential that the mixed fraction of environmental air into a positively buoyant cloud parcel is sufficiently small so that the parcel will remain positively buoyant with an updraft velocity. Because of

adiabatic expansion, RH will increase in such a rising parcel.

In the case of homogeneous mixing, the environmental and cloudy air mix instantaneously. Because of the reduction in droplet size and number concentration, the adjusted S_{qs} will be larger than its initial value before the mixing process. The largest and most hygroscopic CCN, which were transported into the cloud during the entrainment process, likely have a critical supersaturation below S_{qs} and will be activated.

During inhomogeneous mixing, a large portion of the environmental air that is mixed into the cloud remains separated from the cloudy air for the time span of the turbulent mixing time scale τ_t. As the entrained parcel rises, a linear increase in RH in this parcel occurs, because there are no droplets to act as sinks. If the environmental air is sufficiently humid (close to saturation, as was observed during the measurements), then RH could reach 100% and beyond, which leads to the activation of CCN until the number of droplets is large enough to deplete the supersaturation and relax to a quasi-steady value. The progress of this process is limited by τ_t, w of the cloud, and the initial RH of the entrained air. It is possible to estimate the maximum increase in supersaturation during one eddy turnover by looking at the equation for evolution of supersaturation: $dS/dt = a_0 w - bN(\overline{D}/2)S$. Because of dilution and complete evaporation of the cloud droplets, the equation will reduce to $dS/dt = a_0 w$. We assume that $dt = \tau_t$, where $\tau_t = (L_E^2/\varepsilon)^{1/3}$ is the time needed for an eddy with initial dimension L_E to be completely mixed in a turbulent environment with the local energy dissipation rate ε. Assuming $L_E = 100$ m and $\varepsilon = 10^{-3}$ m^2 s^{-3}, as well as $w = 1$ m s^{-1} and $a_0 = 5 \times 10^{-4}$ s^{-1}, an increase of 10% in S can be reasonably expected during one mixing time scale. Therefore, especially if almost-saturated air is mixed into the cloud, saturation can plausibly be reached and supersaturations adequate for secondary activation can be produced.

Figure 4d shows a profile of the difference between the mean volume diameter $\overline{D_v}$ and the arithmetic-mean droplet diameter $\overline{D}$ for the actively growing and the dissolving clouds. For the dissolving stage, this difference increases with height, which indicates that the number of small cloud droplets increases significantly with height, compared to the active stage. This provides evidence that secondary activation takes place at some point in the evolution of the observed dissolving clouds.

Krueger (2008) studied the entrainment mixing process using an Explicit Mixing Parcel Model, which calculates the growth of thousands of individual droplets based on each droplet's local environment. By entraining CCN with a number concentration identical to the CCN concentration at cloud base, as well as subsequent lifting of the mixed parcel, similar results were obtained as in Figs. 6d and 6e. In their case [Fig. 12 in Krueger (2008)] the normalized droplet size also decreased to about 0.4, whereas the droplet number was close to that expected in an adiabatic parcel.

Even without mixing, secondary activation would be possible if there were some larger cloud droplets that can serve as collector droplets in the cloud. By collision and coalescence with smaller cloud droplets, N would be reduced, which would again lead to an increase in S_{qs} (Pontikis and Hicks 1993). Of the observed clouds that showed signs of secondary activation, 65% showed also broad size distributions containing some droplets with diameters greater than 50 μm.

b. Humid shells

Another explanation of the observed large changes in LWC and N but nearly constant D_v in Fig. 3 is the entrainment of nearly saturated air. Similar results were obtained by Paluch and Knight (1984), Blyth and Latham (1990), and Gerber et al. (2008), who found a predominance of large changes in LWC accompanied by steady values of D_v (or effective radius r_e). Entrainment of environmental air that is almost saturated results in only minor evaporation of cloud droplets in the mixing zone (Burnet and Brenguier 2007; Gerber et al. 2008), and the mixing process reduces to simple dilution. To corroborate this idea, the cloud environment is investigated in terms of a possible humid shell surrounding the cloud. Such shells—also called humidity halos—have been observed by aircraft measurements (e.g., Malkus 1949; Ackerman 1958; Perry and Hobbs 1996; Lu et al. 2003; Laird 2005) and by modeling studies (e.g., Slawinska et al. 2012) and seem to be typical features of trade wind cumuli.

Figure 9 shows a cross section of w (black line) and the absolute humidity a (blue line) in representative clouds at the actively growing and dissolving stage. The cloud in terms of LWC is shown as a gray area, and the edges of each cloud are marked by a solid vertical line. It is quite obvious that, for each cloud, a region directly adjacent to the cloud edges is found, where a is still relatively high compared to environmental values. That is, the clouds are surrounded by a humid shell with a horizontal dimension on the order of a few tens of meters.

As a first step, we are interested in the general existence of such a humid shell for the different cloud stages. Therefore, the following simple criteria are applied to identify a humid shell: the shell has to be positioned in the downdraft area outside the cloud (LWC < 0.02 g m^{-3}), and a has to be larger than the median value of a in the nearby cloud-free environment. In Fig. 9, this
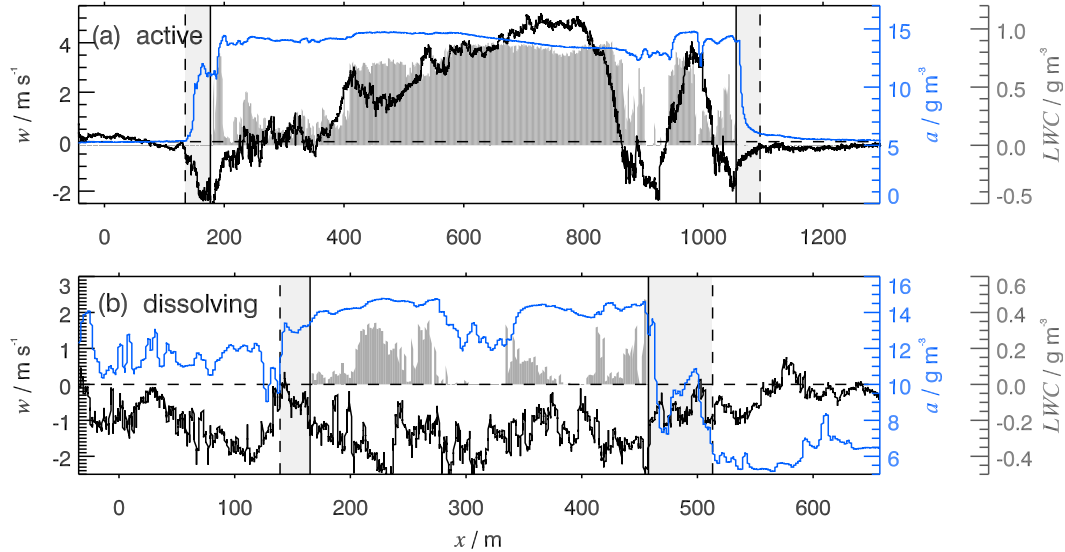
FIG. 9. Cross section through (a) an actively growing cloud and (b) a dissolving cloud showing LWC (gray bars), vertical velocity (black line), and absolute humidity (blue line). Solid vertical lines mark the edges of the cloud and the dashed lines mark the edges of the humid shell. The light-gray-shaded rectangles represent the region of the humid shell.

humid shell region is shaded light gray in the graphics, and its end is marked by a dashed vertical line. The horizontal extent of these shells is highly variable and ranges from 20 to 1000 m and also differs for downshear and upshear sides of the cloud.

To study the humid shells statistically, the 90th percentile of the absolute humidity in the shell a_{shell} is related to the 90th percentile of a in the cloud interior a_{int} by taking into account the median of the environmental value of a (a_{env}):

$$\beta = \frac{a_{shell} - a_{env}}{a_{int} - a_{env}}. \qquad (12)$$

In the case of $\beta = 0$ there is no humid shell for the respective cloud, whereas $\beta = 1$ indicates that the shell is as humid as the cloud interior. The ratio β is independent of differences in the measurement heights and the general day-to-day variability of cloud measurements. Figure 10 shows the PDFs of β for the actively growing and the dissolving cloud stage. The active clouds cover the whole range of β values with broad peaks ranging from 0.6 to 0.8. The dissolving clouds show no values of $\beta < 0.1$ and a distinct peak at about $\beta = 0.75$. The mean values of 0.56 and 0.63 indicate that the region around the clouds is, on average, more humid than the farther-away cloud-free environment. Also, this region becomes slightly more humid as the clouds transition from the active to the dissolving stage.

Closely linked to humid shells are what are commonly referred to as subsiding shells (Telford and Warner 1962). Heus and Jonker (2008) analyzed subsiding shells around shallow cumuli using LES, and Katzwinkel et al. (2014) observed such shells around shallow cumuli sampled during CARRIBA. Both found that the horizontal extension of these subsiding shells increases with increasing cloud age.

To analyze the horizontal extent of the humid shell around the cloud at a certain height level, the approach presented by Perry and Hobbs (1996) is used. The humidity around the cloud is expressed as decaying exponentially from the average absolute humidity in the cloud interior $\overline{a}_{cloud}$ to the average absolute humidity in the cloud-free environment a_{env}, which is not influenced by the subsiding shell. Therefore, a at the outer edge of the humid shell is arbitrarily defined based on the e-folding decay of the profile of a, and the humid shell is the region in which a around the cloud exceeds the e-folding value a_e:

$$a_e(z) = \overline{a}_{cloud}(z) - \{[\overline{a}_{cloud}(z) - \overline{a}_{env}(z)](1 - e^{-1})\}. \qquad (13)$$

We are aware of the problem that not all humid shells follow exactly an exponential function, but a more detailed study of the shell width is beyond the scope of this paper. The width of the humid shell is shown in Fig. 11 for the actively growing and dissolving cloud stage in terms of a box-and-whisker plot. The median shell width differs significantly for the two cloud evolutionary stages with a median width of approximately 30 m corresponding
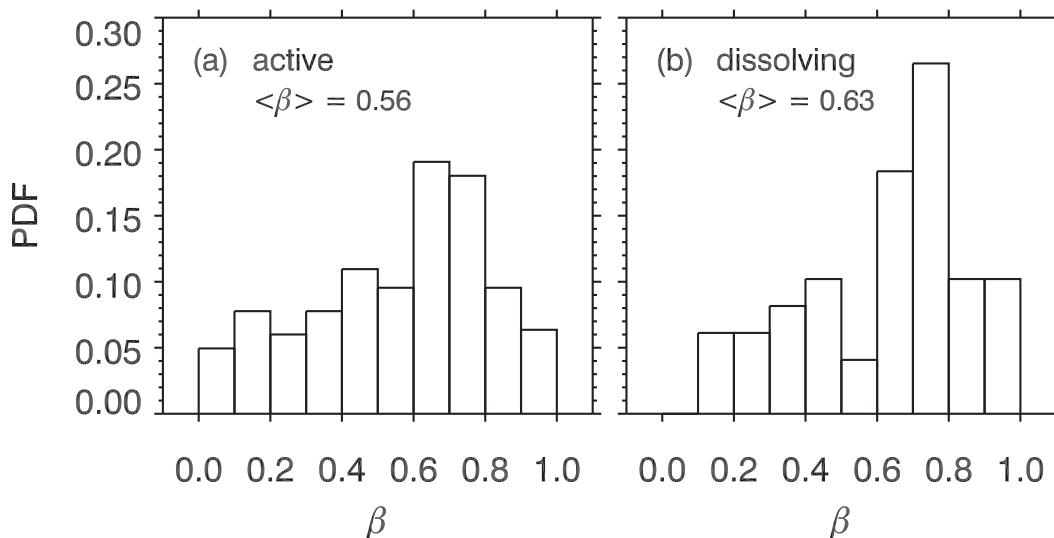
FIG. 10. PDF of $\beta = (a_{shell} - a_{env})/(a_{int} - a_{env})$, where a_{shell} is the 90th percentile of the absolute humidity a in the humid shell around the cloud, a_{int} is the 90th percentile of a in the interior of the cloud, and a_{env} is the median value of a in the cloud-free environment. The distribution as well as the mean value of β is given for (a) actively growing clouds and (b) dissolving clouds.

to the dissolving stage. The actively growing clouds show a comparably small median width of about 0.8 m. The minimum and maximum values show a strong increase of about two orders of magnitude during the transition from the active to the dissolving clouds. The maximum observed width of the humid shell exceeds 100 m for the dissolving cloud stage. These results agree well with the findings from Heus and Jonker (2008) and Katzwinkel et al. (2014). An analysis of the impact of shear on the shell width did not yield any clear results and is therefore not included in the analysis.

As the humid shells grow to the length of L_E, the mixing of entrained air approaches pure dilution with no evaporation taking place. If the entrained air parcel experiences lifting, then secondary activation is very likely to occur because of the very high RH. Therefore, the existence of broad humid shells as observed for the dissolving clouds favor the process of secondary activation. Because of the generally negative vertical velocity associated with dissolving clouds, this can only occur locally.

It is often stated that it is impossible to distinguish between homogeneous and inhomogeneous mixing if the environmental air is close to saturation. The classical picture of inhomogeneous mixing is entrainment of unmodified environmental air and subsequent complete evaporation of portions of the cloud, while the cloud core is preserved, until the mixture of clear but humidified air is able to mix thoroughly with the cloudy air. The result is simple dilution on the mixing diagram. The humid shell can be viewed as the product of that initial

stage of inhomogeneous mixing, and the subsequent mixing of humid-shell air with the cloud can be viewed as the final stage of inhomogeneous mixing. Therefore, we consider the humid shell as part of the inhomogeneous mixing process. This is consistent with the schematic of Fig. 8 in Katzwinkel et al. (2014), where the evolution of the different cloud regions over time is illustrated.

6. Summary

The mixing process of environmental air into shallow trade wind cumuli is analyzed based on data sampled during the CARRIBA campaign in November 2010 near Barbados. The analysis is based on helicopter-borne measurements performed with the payload
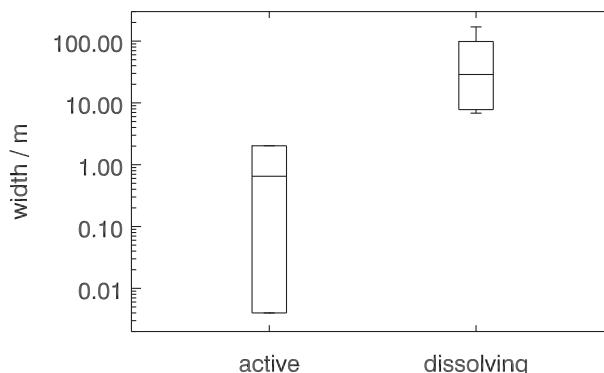

FIG. 11. Box-and-whisker plot of the width of the humid shell around the clouds obtained for actively growing and dissolving clouds.

ACTOS with a spatial resolution in the decimeter range. The investigated clouds were classified into three stages of their life cycle according to criteria based on vertical velocity w and buoyancy acceleration B in the cloud interior (Katzwinkel et al. 2014). A dataset of 177 actively growing, 91 decelerating, and 32 dissolving clouds has been identified, and this study focuses on the actively growing and dissolving stage. This work presents the first detailed analysis of cloud microphysical response to entrainment as a function of cloud evolutionary stage.

It is found that the cloud droplet number concentration N and cloud liquid water content (LWC) decrease strongly during the transition from the active to the dissolving stage. This decrease occurs in the cloud interior as well as in the edge region of the clouds. The mean volume diameter D_v in contrast shows only a small decrease. This behavior is attributed to the presence of humidity shells around the observed clouds, which reduce the evaporation of cloud droplets during the entrainment and mixing. These areas of enhanced humidity increase in horizontal extent as the clouds transition from the active to the dissolving stages. No significant broadening of the cloud droplet number size distribution is observed during the transition from the active to the dissolving cloud stage.

Signs of secondary droplet activation are found in the droplet size distributions for about 46% of the observed clouds. It is found that there is a significant tendency from homogeneous mixing of actively growing clouds to more inhomogeneous mixing with increasing cloud life time, when only looking at clouds with purely monomodal size distributions. This is derived from mixing diagrams of individual clouds, as well as from two statistical analyses. These findings are supported by previous observations of shear-induced turbulence at the edges of actively growing clouds (e.g., Siebert et al. 2006b). This increased local turbulence results in a reduced mixing time scale, which favors homogeneous mixing. Also, indications of an active collision–coalescence process were found in some clouds. Both secondary activation and collision–coalescence make the interpretation of mixing diagrams more complex. The additional droplet source/sink leads under certain conditions to somewhat ambiguous results, and further investigation of this important problem is needed.

REFERENCES

Ackerman, B., 1958: Turbulence around tropical cumuli. *J. Meteor.,* **15,** 69–74, doi:10.1175/1520-0469(1958)015<0069:TATC>2.0.CO;2.

Arabas, S., H. Pawlowska, and W. W. Grabowski, 2009: Effective radius and droplet spectral width from in-situ aircraft observations in trade-wind cumuli during RICO. *Geophys. Res. Lett.,* **36,** L11803, doi:10.1029/2009GL038257.

Austin, P. H., M. B. Baker, A. M. Blyth, and J. B. Jensen, 1985: Small-scale variability in warm continental cumulus clouds. *J. Atmos. Sci.,* **42,** 1123–1138, doi:10.1175/1520-0469(1985)042<1123:SSVIWC>2.0.CO;2.

Baker, M. B., and J. Latham, 1979: The evolution of droplet spectra and the rate of production of embryonic raindrops in small cumulus clouds. *J. Atmos. Sci.,* **36,** 1612–1615, doi:10.1175/1520-0469(1979)036<1612:TEODSA>2.0.CO;2.

——, R. G. Corbin, and J. Latham, 1980: The influence of entrainment on the evolution of cloud droplet spectra. I: A model of inhomogeneous mixing. *Quart. J. Roy. Meteor. Soc.,* **106,** 581–598, doi:10.1002/qj.49710644914.

——, R. E. Breidenthal, T. W. Choularton, and J. Latham, 1984: The effects of turbulent mixing in clouds. *J. Atmos. Sci.,* **41,** 299–304, doi:10.1175/1520-0469(1984)041<0299:TEOTMI>2.0.CO;2.

Blyth, A. M., and J. Latham, 1990: Airborne studies of the altitudinal variability of the microphysical structure of small, ice-free, montanan cumulus clouds. *Quart. J. Roy. Meteor. Soc.,* **116,** 1405–1423, doi:10.1002/qj.49711649608.

Brenguier, J.-L., and L. Chaumat, 2001: Droplet spectra broadening in cumulus clouds. Part I: Broadening in adiabatic cores. *J. Atmos. Sci.,* **58,** 628–641, doi:10.1175/1520-0469(2001)058<0628:DSBICC>2.0.CO;2.

——, H. Pawlowska, L. Schüller, R. Preusker, J. Fischer, and Y. Fouquart, 2000: Radiative properties of boundary layer clouds: Droplet effective radius versus number concentration. *J. Atmos. Sci.,* **57,** 803–821, doi:10.1175/1520-0469(2000)057<0803:RPOBLC>2.0.CO;2.

Bretherton, C. S., J. R. McCaa, and H. Grenier, 2004: A new parametrization for shallow cumulus convection and its application to marine subtropical cloud-topped boundary layers. Part I: Description and 1D results. *Mon. Wea. Rev.,* **132,** 864–882, doi:10.1175/1520-0493(2004)132<0864:ANPFSC>2.0.CO;2.

Burnet, F., and J.-L. Brenguier, 2007: Observational study of the entrainment-mixing process in warm convective clouds. *J. Atmos. Sci.,* **64,** 1995–2011, doi:10.1175/JAS3928.1.

Chuang, P. Y., E. W. Saw, J. D. Small, R. A. Shaw, C. M. Sipperley, G. A. Payne, and W. Bachalo, 2008: Airborne phase Doppler interferometry for cloud microphysical measurements. *Aerosol Sci. Technol.,* **42,** 685–703, doi:10.1080/02786820802232956.

Cooper, W. A., 1989: Effects of variable droplet growth histories on droplet size distributions. Part I: Theory. *J. Atmos. Sci.,* **46,** 1301–1311, doi:10.1175/1520-0469(1989)046<1301:EOVDGH>2.0.CO;2.

Ditas, F., 2014: Microphysical properties of aerosol particles in the trade wind regime and their influence on the number

concentration of activated particles in trade wind cumulus clouds. Ph.D. thesis, University of Leipzig, 113 pp.

Feingold, G., L. A. Remer, J. Ramaprasad, and Y. J. Kaufman, 2001: Analysis of smoke impact on clouds in Brazilian biomass burning regions: An extension of Twomey's approach. *J. Geophys. Res.,* **106,** 22 907–22 922, doi:10.1029/2001JD000732.

Gerber, H., 2006: Entrainment, mixing, and microphysics in RICO cumulus. *12th Conf. on Cloud Physics,* Madison, WI, Amer. Meteor. Soc., 14.2A. [Available online at https://ams.confex.com/ams/pdfpapers/109676.pdf.]

——, G. M. Frick, J. B. Jensen, and J. G. Hudson, 2008: Entrainment, mixing, and microphysics in trade-wind cumulus. *J. Meteor. Soc. Japan,* **86A,** 87–106, doi:10.2151/jmsj.86A.87.

Grabowski, W., 2006: Indirect impact of atmospheric aerosols in idealized simulations of convective–radiative quasi equilibrium. *J. Climate,* **19,** 4664–4682, doi:10.1175/JCLI3857.1.

Haman, K. E., A. Makulski, S. P. Malinowski, and R. Busen, 1997: A new ultrafast thermometer for airborne measurements in clouds. *J. Atmos. Oceanic Technol.,* **14,** 217–227, doi:10.1175/1520-0426(1997)014<0217:ANUTFA>2.0.CO;2.

Heus, T., and H. J. J. Jonker, 2008: Subsiding shells around shallow cumulus clouds. *J. Atmos. Sci.,* **65,** 1003–1018, doi:10.1175/2007JAS2322.1.

Hill, T. A., and T. W. Choularton, 1985: An airborne study of the microphysical structure of cumulus clouds. *Quart. J. Roy. Meteor. Soc.,* **111,** 517–544, doi:10.1002/qj.49711146813.

Jarecka, D., W. W. Grabowski, H. Morrison, and H. Pawlowska, 2013: Homogeneity of the subgrid-scale turbulent mixing in large-eddy simulation of shallow convection. *J. Atmos. Sci.,* **70,** 2751–2767, doi:10.1175/JAS-D-13-042.1.

Jensen, J. B., and M. B. Baker, 1989: A simple model for droplet spectra evolution during turbulent mixing. *J. Atmos. Sci.,* **46,** 2812–2829, doi:10.1175/1520-0469(1989)046<2812:ASMODS>2.0.CO;2.

——, P. H. Austin, M. B. Baker, and A. M. Blyth, 1985: Turbulent mixing, spectral evolution and dynamics in a warm cumulus cloud. *J. Atmos. Sci.,* **42,** 173–192, doi:10.1175/1520-0469(1985)042<0173:TMSEAD>2.0.CO;2.

Kain, J. S., and J. M. Fritsch, 1990: A one-dimensional entraining/detraining plume model and its application in convective parameterization. *J. Atmos. Sci.,* **47,** 2784–2802, doi:10.1175/1520-0469(1990)047<2784:AODEPM>2.0.CO;2.

Katzwinkel, J., H. Siebert, T. Heus, and R. A. Shaw, 2014: Measurements of turbulent mixing and subsiding shells in trade wind cumuli. *J. Atmos. Sci.,* **71,** 2810–2822, doi:10.1175/JAS-D-13-0222.1.

Korolev, A. V., and I. P. Mazin, 2003: Supersaturation of water vapor in clouds. *J. Atmos. Sci.,* **60,** 2957–2974, doi:10.1175/1520-0469(2003)060<2957:SOWVIC>2.0.CO;2.

Krueger, S., 2008: Fine-scale modeling of entrainment and mixing of cloudy and clear air. *Extended Abstract, 15th Int. Conf. on Clouds and Precipitation,* Cancun, Mexico, Int. Commission on Clouds and Precipitation, P1.10. [Available online at http://cabernet.atmosfcu.unam.mx/ICCP-2008/abstracts/Program_on_line/Poster_01/Krueger_extended.pdf.]

Kumar, B., J. Schumacher, and R. A. Shaw, 2013: Cloud microphysical effects of turbulent mixing and entrainment. *Theor. Comput. Fluid Dyn.,* **27,** 361–376, doi:10.1007/s00162-012-0272-z.

Laird, N. F., 2005: Humidity halos surrounding small cumulus clouds in a tropical environment. *J. Atmos. Sci.,* **62,** 3420–3425, doi:10.1175/JAS3538.1.

Lehmann, K., H. Siebert, and R. A. Shaw, 2009: Homogeneous and inhomogeneous mixing in cumulus clouds: Dependence on

local turbulence structure. *J. Atmos. Sci.,* **66,** 3641–3659, doi:10.1175/2009JAS3012.1.

Lu, M.-L., J. Wang, A. Freedman, H. H. Jonsson, R. C. Flagan, R. A. McClatchey, and J. H. Seinfeld, 2003: Analysis of humidity halos around trade wind cumulus clouds. *J. Atmos. Sci.,* **60,** 1041–1059, doi:10.1175/1520-0469(2003)60<1041:AOHHAT>2.0.CO;2.

Malkus, J. S., 1949: Effects of wind shear on some aspects of convection. *Eos, Trans. Amer. Geophys. Union,* **30,** 19–25, doi:10.1029/TR030i001p00019.

Nuijens, L., I. Serikov, L. Hirsch, K. Lonitz, and B. Stevens, 2014: The distribution and variability of low-level cloud in the North Atlantic trades. *Quart. J. Roy. Meteor. Soc.,* **140,** 2364–2374, doi:10.1002/qj.2307.

Paluch, I. R., and C. A. Knight, 1984: Mixing and the evolution of cloud droplet size spectra in a vigorous continental cumulus. *J. Atmos. Sci.,* **41,** 1801–1815, doi:10.1175/1520-0469(1984)041<1801:MATEOC>2.0.CO;2.

——, and D. G. Baumgardner, 1989: Entrainment and fine-scale mixing in a continental convective cloud. *J. Atmos. Sci.,* **46,** 261–278, doi:10.1175/1520-0469(1989)046<0261:EAFSMI>2.0.CO;2.

Pawlowska, H., J.-L. Brenguier, and F. Burnet, 2000: Microphysical properties of stratocumulus clouds. *Atmos. Res.,* **55,** 15–33, doi:10.1016/S0169-8095(00)00054-5.

Perry, K. D., and P. V. Hobbs, 1996: Influences of isolated clouds on the humidity of their surroundings. *J. Atmos. Sci.,* **53,** 159–174, doi:10.1175/1520-0469(1996)053<0159:IOICCO>2.0.CO;2.

Pontikis, C., and E. Hicks, 1993: Droplet activation as related to entrainment and mixing in warm tropical maritime clouds. *J. Atmos. Sci.,* **50,** 1888–1896, doi:10.1175/1520-0469(1993)050<1888:DAARTE>2.0.CO;2.

Riehl, H., T. Yeh, J. S. Malkus, and N. la Seur, 1951: The north-east trade of the Pacific Ocean. *Quart. J. Roy. Meteor. Soc.,* **77,** 598–626, doi:10.1002/qj.49707733405.

Roberts, G. C., and A. Nenes, 2005: A continuous-flow streamwise thermal-gradient CCN chamber for atmospheric measurements. *Aerosol Sci. Technol.,* **39,** 206–221, doi:10.1080/027868290913988.

Rogers, R. R., and M. K. Yau, 1989: *A Short Course in Cloud Physics.* 3rd ed. Pergamon Press, 293 pp.

Siebert, H., H. Franke, K. Lehmann, R. Maser, E. W. Saw, D. Schell, R. A. Shaw, and M. Wendisch, 2006a: Probing finescale dynamics and microphysics of clouds with helicopter-borne measurements. *Bull. Amer. Meteor. Soc.,* **87,** 1727–1738, doi:10.1175/BAMS-87-12-1727.

——, K. Lehmann, M. Wendisch, and R. Shaw, 2006b: Small-scale turbulence in clouds. *12th Conf. on Cloud Physics,* Madison, WI, Amer. Meteor. Soc., 12.1. [Available online at https://ams.confex.com/ams/Madison2006/techprogram/paper_112465.htm.]

——, and Coauthors, 2013: The fine-scale structure of the trade wind cumuli over Barbados—An introduction to the CARRIBA project. *Atmos. Chem. Phys.,* **13,** 10 061–10 077, doi:10.5194/acp-13-10061-2013.

Slawinska, J., W. Grabowski, H. Pawlowska, and H. Morrison, 2012: Droplet activation and mixing in large-eddy simulation of a shallow cumulus field. *J. Atmos. Sci.,* **69,** 444–462, doi:10.1175/JAS-D-11-054.1.

Small, J. D., P. Y. Chuang, and H. H. Jonsson, 2013: Microphysical imprint of entrainment in warm cumulus. *Tellus,* **65B,** 19 922, doi:10.3402/tellusb.v65i0.19922.

Squires, P., 1958: Penetrative downdraughts in cumuli. *Tellus,* **10A,** 381–389, doi:10.1111/j.2153-3490.1958.tb02025.x.

——, and J. Warner, 1957: Some measurement in the orographic cloud of the island of Hawaii and in trade wind cumuli. *Tellus,* **9A,** 475–494, doi:10.1111/j.2153-3490.1957.tb01909.x.

Stevens, B., 2005: Atmospheric moist convection. *Annu. Rev. Earth Planet. Sci.,* **33,** 605–643, doi:10.1146/annurev.earth.33.092203.122658.

Stith, J., and M. Politovich, 1989: Observations of the effects of entrainment and mixing on the droplet size spectra in a small cumulus. *J. Atmos. Sci.,* **46,** 908–919, doi:10.1175/1520-0469(1989)046<0908:OOTEOE>2.0.CO;2.

Stommel, H., 1947: Entrainment of air into a cumulus cloud. *J. Meteor.,* **4,** 91–94, doi:10.1175/1520-0469(1947)004<0091:EOAIAC>2.0.CO;2.

Su, C.-W., K. Krueger, P. A. McMurtry, and P. H. Austin, 1998: Linear eddy modeling of droplet spectral evolution during entrainment and mixing in cumulus clouds. *Atmos. Res.,* **47–48,** 41–58, doi:10.1016/S0169-8095(98)00039-8.

Telford, J. W., and J. Warner, 1962: On the measurement from an aircraft of bouyancy and vertical air velocity in cloud. *J. Atmos. Sci.,* **19,** 415–423, doi:10.1175/1520-0469(1962)019<0415:OTMFAA>2.0.CO;2.

——, and S. K. Chai, 1980: A new aspect of condensation theory. *Pure Appl. Geophys.,* **118,** 720–742, doi:10.1007/BF01593025.

Tiedtke, M., 1989: A comprehensive mass flux scheme for cumulus parameterization in large-scale models. *Mon. Wea. Rev.,* **117,** 1779–1800, doi:10.1175/1520-0493(1989)117<1779:ACMFSF>2.0.CO;2.

Topping, D., P. Connolly, and G. McFiggans, 2013: Cloud droplet number enhanced by co-condensation of organic vapours. *Nature Geosci.,* **6,** 443–446, doi:10.1038/ngeo1809.

Warner, J., 1955: The water content of cumuliform clouds. *Tellus,* **7A,** 449–457, doi:10.1111/j.2153-3490.1955.tb01183.x.

——, 1969: The microstructure of cumulus cloud. Part I: General features of the droplet spectrum. *J. Atmos. Sci.,* **26,** 1049–1059, doi:10.1175/1520-0469(1969)026<1049:TMOCCP>2.0.CO;2.

Wendisch, M., and J.-L. Brenguier, 2013: *Airborne Measurements for Environmental Research: Methods and Instruments*. Wiley, 641 pp.

Werner, F., H. Siebert, P. Pilewskie, T. Schmeissner, R. A. Shaw, and M. Wendisch, 2013: New airborne retrieval approach for trade wind cumulus properties under overlying cirrus. *J. Geophys. Res. Atmos.,* **118,** 3634–3649, doi:10.1002/jgrd.50334.

——, and Coauthors, 2014: Twomey effect observed from collocated microphysical and remote sensing measurements over shallow cumulus. *J. Geophys. Res. Atmos.,* **119,** 1534–1545, doi:10.1002/2013JD020131.